High-density multi-fiber photometry for studying large-scale brain circuit dynamics

Sych, Yaroslav ; Chernysheva, Maria ; Sumanovski, Lazar T ; Helmchen, Fritjof

Abstract: Animal behavior originates from neuronal activity distributed across brain-wide networks. However, techniques available to assess large-scale neural dynamics in behaving animals remain limited. Here we present compact, chronically implantable, high-density arrays of optical fibers that enable multi-fiber photometry and optogenetic perturbations across many regions in the mammalian brain. In mice engaged in a texture discrimination task, we achieved simultaneous photometric calcium recordings from networks of 12-48 brain regions, including striatal, thalamic, hippocampal and cortical areas. Furthermore, we optically perturbed subsets of regions in VGAT-ChR2 mice by targeting specific fiber channels with a spatial light modulator. Perturbation of ventral thalamic nuclei caused distributed network modulation and behavioral deficits. Finally, we demonstrate multi-fiber photometry in freely moving animals, including simultaneous recordings from two mice during social interaction. High-density multi-fiber arrays are versatile tools for the investigation of large-scale brain dynamics during behavior.

DOI: https://doi.org/10.1038/s41592-019-0400-4

nature methods

ARTICLES

https://doi.org/10.1038/s41592-019-0400-4

High-density multi-fiber photometry for studying large-scale brain circuit dynamics

Yaroslav Sych[1*], Maria Chernysheva[1,2], Lazar T. Sumanovski[1] and Fritjof Helmchen[1,2*]

Animal behavior originates from neuronal activity distributed across brain-wide networks. However, techniques available to assess large-scale neural dynamics in behaving animals remain limited. Here we present compact, chronically implantable, high-density arrays of optical fibers that enable multi-fiber photometry and optogenetic perturbations across many regions in the mammalian brain. In mice engaged in a texture discrimination task, we achieved simultaneous photometric calcium recordings from networks of 12–48 brain regions, including striatal, thalamic, hippocampal and cortical areas. Furthermore, we optically perturbed subsets of regions in VGAT-ChR2 mice by targeting specific fiber channels with a spatial light modulator. Perturbation of ventral thalamic nuclei caused distributed network modulation and behavioral deficits. Finally, we demonstrate multi-fiber photometry in freely moving animals, including simultaneous recordings from two mice during social interaction. High-density multi-fiber arrays are versatile tools for the investigation of large-scale brain dynamics during behavior.

Neural substrates of complex behaviors involve large neuronal ensembles distributed across multiple brain areas. Whereas whole-brain imaging has become feasible in the small brains of *Caenorhabditis elegans*[1], *Drosophila*[2] and zebrafish larvae[1,3], methods available to investigate distributed neural activity in the mammalian brain, especially during behavior, remain limited. Functional magnetic resonance imaging (fMRI), which infers neural activity indirectly from blood flow changes, suffers from low spatiotemporal fidelity and is difficult to apply to behaving animals. Functional ultrasound imaging[4] provides improved temporal resolution but primarily measures microvasculature dynamics. Electrophysiological approaches either record surface signals (as for electroencephalography) or—with electrodes inserted deeply—measure local field potentials and multi- or single-unit activity. Although the latter approaches were recently scaled up by multi-site local field potential recordings[5] and with Neuropixels silicon probes[6], dissection of the contribution of distinct cell types remains problematic. Optical imaging approaches, combined with modern genetic tools[7], can provide cell-type specificity and complement electrophysiological methods. Recently, imaging techniques were extended to larger scales through the development of two-photon mesoscopes providing cellular resolution across multiple regions within millimeter-sized fields of view[8–11]. These systems are, however, technically sophisticated. Wide-field camera imaging is an alternative—for example, using one-photon excitation of calcium or voltage indicators in transgenic mice[12–15]—but sacrifices cellular resolution. To date, both approaches have been applied mainly to the brain surface, whereas subcortical imaging through inserted gradient-index lenses[16] has typically targeted only individual deep brain regions. It is therefore desirable to expand large-scale optical recordings to the broader subcortical realm, where many brain nuclei execute essential functions.

A simple method to optically record from subcortical regions is fiber photometry, in which bulk fluorescence signals are excited and collected at the tip of an optical fiber[17–19]. Although it lacks cellular resolution, fiber photometry has gained considerable attention because of its simplicity, its versatility and the potential to chronically implant fibers into brain tissue. Its combination with cell-type- or pathway-specific expression of genetically encoded calcium or voltage indicators[19–21] is particularly powerful, and optical fibers are also commonly used for optogenetic perturbations[22,23]. Fiber photometry is potentially scalable to allow brain-wide measurements and manipulations. Two previous studies demonstrated fiber photometry from multiple mouse brain regions (up to seven across both hemispheres)[24,25]. However, the relatively bulky standard ferrules used for single-fiber implants have kept the minimal distance between neighboring fiber implants at 1.25 mm, fundamentally restricting channel density and the flexibility of implant configurations. Higher channel densities are needed to comprehensively explore large-scale functional circuits with their parallel pathways[26] and feed-forward and feedback loops. Eventually, our goal is to cover large parts of the mesoscale brain network[27] with multi-site optical recordings.

Here we introduce high-density, multi-fiber arrays enabling multi-fiber photometry from several tens of brain regions simultaneously. We built arrays with up to 24 fibers and show that single or multiple arrays can be chronically implanted into the mouse brain to target specific sets of regions. We demonstrate simultaneous measurement of calcium dynamics from up to 48 brain regions, and we provide proof of concept for combining multi-fiber photometry with simultaneous multi-site optogenetic perturbations. The multi-fiber arrays complement existing large-scale recording techniques and offer opportunities for further study of functional organization and behavior-related dynamics of mesoscale circuits in the mammalian brain.

Results

Optical setup and high-density multi-fiber arrays. We built an optical setup for parallel fluorescence recordings through multiple optical fibers (Fig. 1a). Fibers (100-µm core) were flexibly held together in 2–3-m-long bundles with their ends fixed in modified fiber array connectors. These fiber ferrules contained guiding grooves for precise alignment of 12, 24 or 48 fibers (Fig. 1b; 250-µm fiber spacing). To excite fluorescence, we coupled laser light into the fiber array at the back end, guided it through the fiber bundle and connected

[1]Brain Research Institute, University of Zurich, Zurich, Switzerland. [2]Neuroscience Center Zurich, Zurich, Switzerland. *e-mail: sych@hifo.uzh.ch; helmchen@hifo.uzh.ch

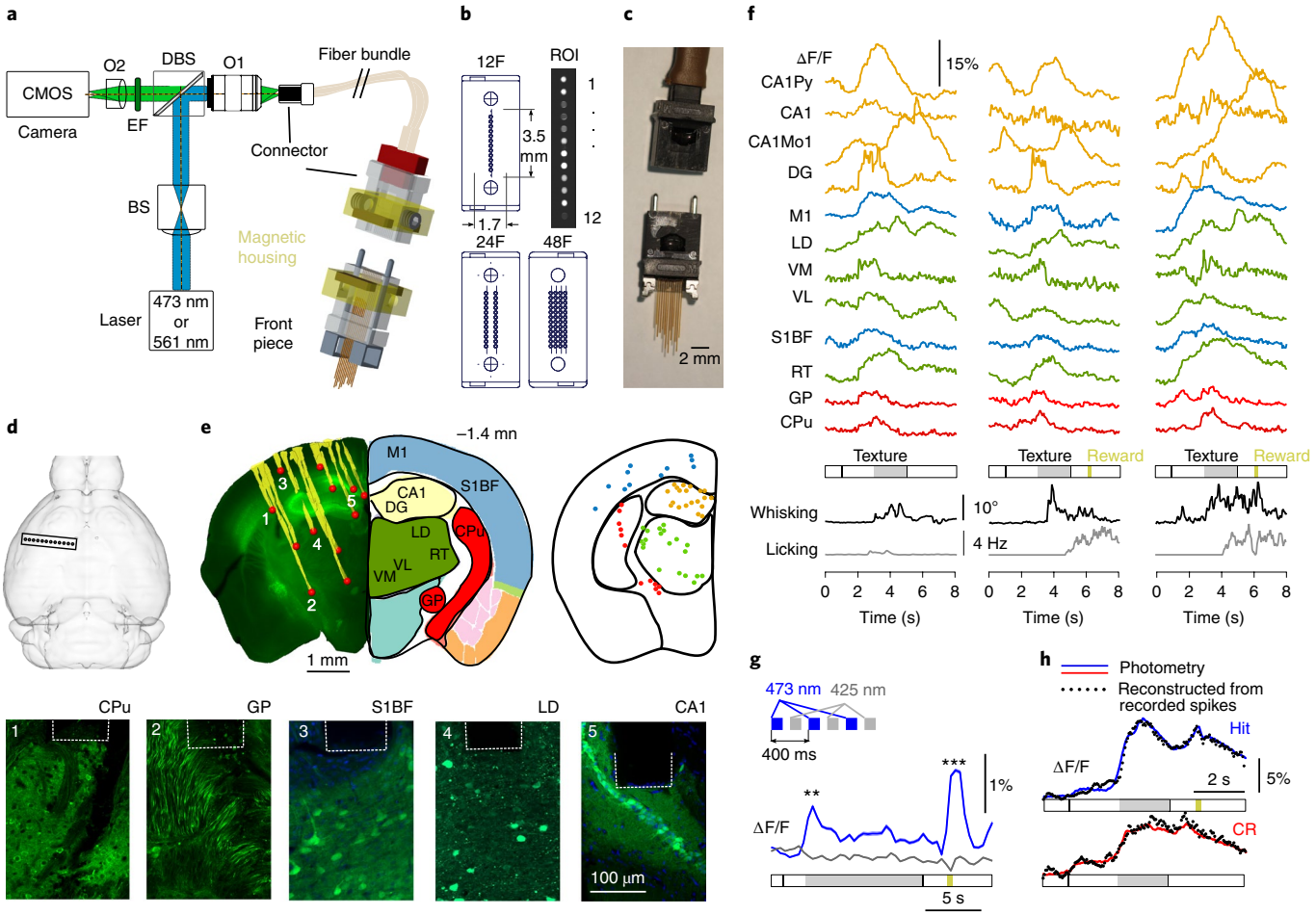

Fig. 1 | Optical setup for multi-site photometry using high-density multi-fiber arrays. a, Schematic setup. A cylindrical lens used as a beam shaper (BS) forms a light sheet at the focal plane of objective 1 (O1). The laser beam is coupled into the fiber bundle connector. A dichroic beam-splitter (DBS) separates excitation and detection pathways, and an emission filter (EF) selects the detected wavelength range. Objective 2 (O2) creates an image of the fiber array on the complementary metal-oxide semiconductor (CMOS) camera sensor. We used 473- and 561-nm lasers to excite GCaMP6m and R-CaMP1.07, respectively. **b**, Dimensions of ferrules holding 12, 24 and 48 fibers (12F, 24F and 48F, respectively). Upper right: example camera image of 12-fiber array end face with GCaMP6m fluorescence. **c**, Photograph of 12-fiber array front piece and fiber bundle connector (without magnetic housing). Front piece dimensions, $7 \times 2.45 \times 8.05\,mm^3$; weight, 0.32 g. **d**, Top view of fiber array implantation geometry. **e**, Left: histology aligned to Allen Brain Atlas[30]. Fiber tracks in yellow with fiber tip positions (red dots) mapped to corresponding brain regions. Right: fiber tip positions for six mice, colored according to targeted brain structures (blue, cortex; red, basal ganglia; green, thalamus; yellow, hippocampus). Bottom: example confocal images of GCaMP6m-expressing cells and axons below individual fiber tips. **f**, ΔF/F traces recorded simultaneously across 12 regions for three example trials (same color-coding as in **e**). Bottom: whisking and licking behaviors. **g**, Mean ΔF/F trace (154 trials) for two-color illumination alternating between 473-nm (blue, calcium-dependent) and 425-nm (gray, calcium-independent) excitation. ΔF/F changes were significantly lower for 425-nm excitation than for 473-nm excitation for 1-s periods during texture touch (**$P = 0.003$, $F = 13.4$; one-way ANOVA) and reward delivery (***$P = 2 \times 10^{-6}$, $F = 23.6$; one-way ANOVA). **h**, Mean ΔF/F signal in M1 for Hit (blue) and CR (red) trials ($n = 112$ and 120, respectively) from opto-tetrode control experiments. A weighted sum of spike rates of single units near the fiber tip reconstructed the observed ΔF/F signals well.

the front end to a front piece that we chronically implanted into the brain. In most cases we used a 12-fiber connector for the front piece (Fig. 1c), but in some experiments we connected separate fiber bundle branches to multiple front pieces, including a 24-fiber front piece (see below). With their solarization-resistant polyimide coating, the fibers exhibited low background fluorescence and elicited minimal tissue immune response (Supplementary Fig. 1). The distal fiber ends (facing the brain) were cut flat and adjusted in length to target specific brain regions (Supplementary Fig. 2). Guiding metal alloy pins and a custom housing with magnetic pins enabled easy attachment and detachment, and ensured precise fiber alignment between connector and front piece. Fluorescence excited at the fiber tips was collected back through the same fiber bundle, and fiber end faces were imaged onto a camera (Fig. 1a,b).

We first implanted six mice with 12-fiber arrays targeting 12 brain regions distributed across basal ganglia, thalamus, hippocampus and neocortex (Fig. 1d). All regions were previously injected with virus expressing the calcium indicator GCaMP6m, and we verified three-dimensional (3D) positions of fiber tips and neuronal labeling in front of these by post hoc histology (Fig. 1e). We simultaneously recorded calcium signals in all targeted brain regions by exciting GCaMP6m fluorescence through all 12 fibers in parallel. On the camera image we selected regions of interest corresponding to the distinct fiber channels for analysis. Mice were head-fixed, awake and engaged in a go/no-go texture discrimination task (see below). Fluorescence changes (ΔF/F) were robust, with up to 20% amplitude and diverse time courses across regions (Fig. 1f). Excitation at 425 nm, nearly isosbestic for GCaMP6, produced flat ΔF/F

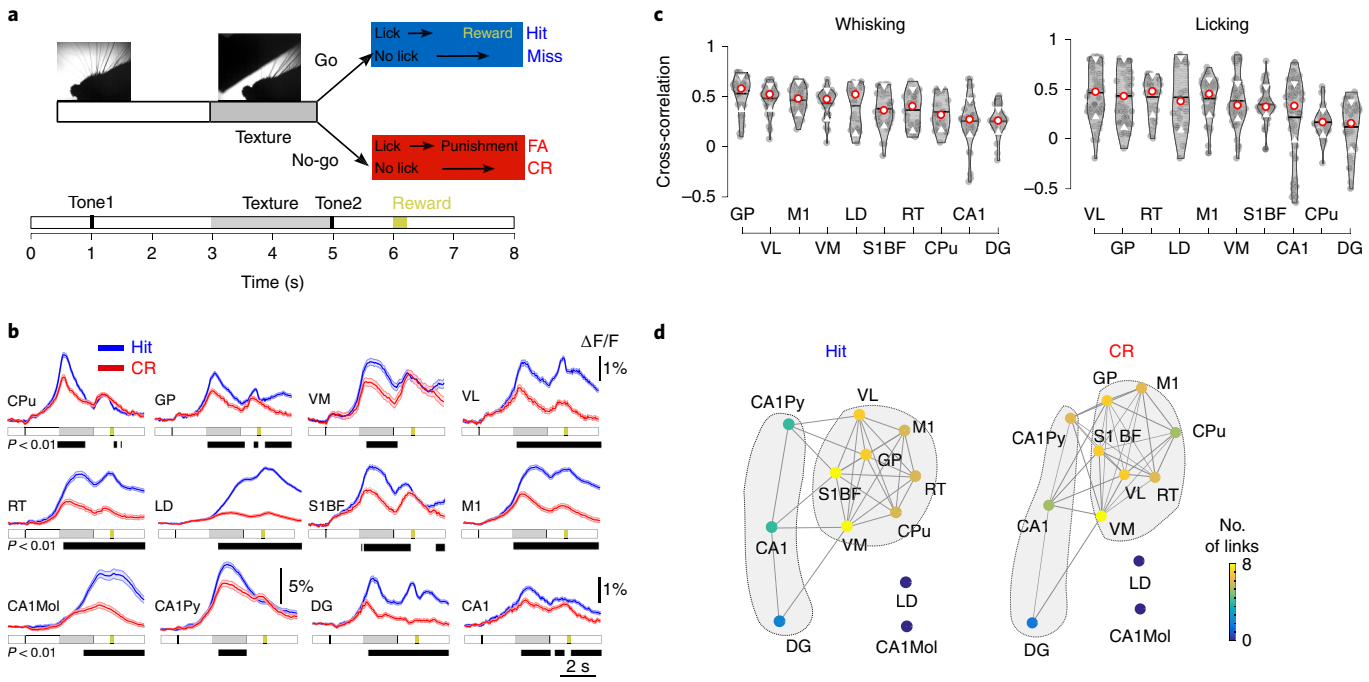

Fig. 2 | Large-scale network dynamics across multiple brain regions during texture discrimination behavior. a, Schematic representation of the go/no-go texture discrimination task. **b**, Example of trial-averaged ΔF/F signals for Hit ($n = 315$ trials) and CR ($n = 323$ trials) (mean ± s.e.m.; gray bars, periods of texture presentation; black bars, periods of significant Hit and CR difference; $P < 0.01$, one-way ANOVA). **c**, Cross-correlations of ΔF/F signals with whisking and licking rates in texture discrimination trials. Distribution contains 34 sessions (5.66 ± 1.22 per mouse, mean ± s.e.m., six mice) at expert performance (>80% correct trials). Median, red circles; mean, black lines; bottom and top notches, 25th and 75th percentile, respectively. **d**, Functional network representation during Hit and CR trials using force-directed placement for the session used to plot **b**. Region nodes are colored according to their number of links. Note that a higher density of links affects spacing between areas—that is, multiple interlinked areas are pulled together into clusters.

traces with substantially lower amplitude than observed with 473-nm excitation ($P < 0.01$, one-way analysis of variance (ANOVA); Fig. 1g), confirming the calcium sensitivity of signals and excluding major contributions of intrinsic signal changes or motion artifacts[24]. We further validated that fiber-optic signals reflect neuronal spiking by simultaneously recording single-unit activity with four tetrodes placed around a single fiber tip. Trial-related ΔF/F signals were well reconstructed by a weighted sum of spike rates recorded from single units near the fiber tip (Fig. 1h, Supplementary Notes and Supplementary Fig. 3). Moreover, we combined photometry with two-photon microscopy and found that brief electrical stimulation of the superficial cortex elicited exponentially decaying calcium transients in GCaMP6m-labeled neurons near the fiber tip, and also produced clear photometric calcium signals (Supplementary Notes and Supplementary Fig. 4). Finally, we verified that signal cross-talk between fiber channels is small—around a few percent for the nearest fiber channels (Supplementary Notes and Supplementary Fig. 5).

Multi-fiber photometry of behavior-related neuronal dynamics in 12–48 brain regions. To exemplify how multi-fiber arrays can be used to assess behavior-related, large-scale circuit dynamics, we tested their application in mice engaged in a whisker-based go/no-go texture discrimination task[28]. Six mice implanted with 12-fiber arrays were habituated to head-fixation and trained to lick for a water reward for one texture type (Hit trials), and to refrain from licking for a non-rewarded different texture (correct rejection (CR) trials) (Fig. 2a). This sensorimotor task probably involves various subcortical regions in basal ganglia, thalamus and hippocampus interacting with neocortical areas[29]. We therefore targeted fiber tips to caudate putamen (CPu) and globus pallidum (GP), to several thalamic nuclei (lateral dorsal (LD), ventral lateral (VL), ventral medial (VM) and reticular nuclei (RT)), to dorsal hippocampal regions (several sublaminae of CA1 and dentate gyrus (DG)) and to neocortical regions (primary somatosensory barrel cortex (S1BF) and posterior part of primary motor cortex (M1)) (a full list of targeted regions is presented in Supplementary Table 1).

In each mouse, we recorded multi-site calcium dynamics, and revealed above-baseline, trial-related ΔF/F signals that in all regions diverged for Hit and CR trials, consistent with discriminability soon after texture touch[9] (Fig. 2b). The time course of calcium signals was diverse and variable across regions, typically showing prominent peaks early following touch (for example, in CPu, GP, VL, DG, S1BF and M1) and/or later during licking and reward retrieval (for example, in LD, GP, VM, VL and CA1). Calcium signals could be stably measured over several weeks (2–6 weeks, six mice) and varied considerably across mice (Supplementary Fig. 6). Calcium signals in VL and GP showed the highest correlations with whisking and licking rates, whereas hippocampal regions (DG, CA1) displayed much weaker correlations (Fig. 2c).

A caveat for the interpretation of fiber-recorded fluorescence signals is that—depending on labeling specificity and local anatomical organization—these potentially represent a weighted sum of signals from somata (and dendrites) and from afferent or passing axons. For example, GP showed dense labeling of axons descending from CPu (Fig. 1e). This problem can be circumvented with pathway-specific labeling strategies, enabling fluorescence recordings from either specific projection neurons or axonal pathways. We exemplify such decomposition of regional calcium signals for GP by using pathway-specific labeling of the CPu→GP and GP→VL pathways, respectively (Supplementary Fig. 7). Keeping this limitation in mind, multi-fiber photometry allows reconstruction of behavior-related functional networks of interacting brain regions. To estimate functional connectivity, we used pairwise correlations between calcium signals[12]. Regions with significant correlation ($P < 0.05$) were

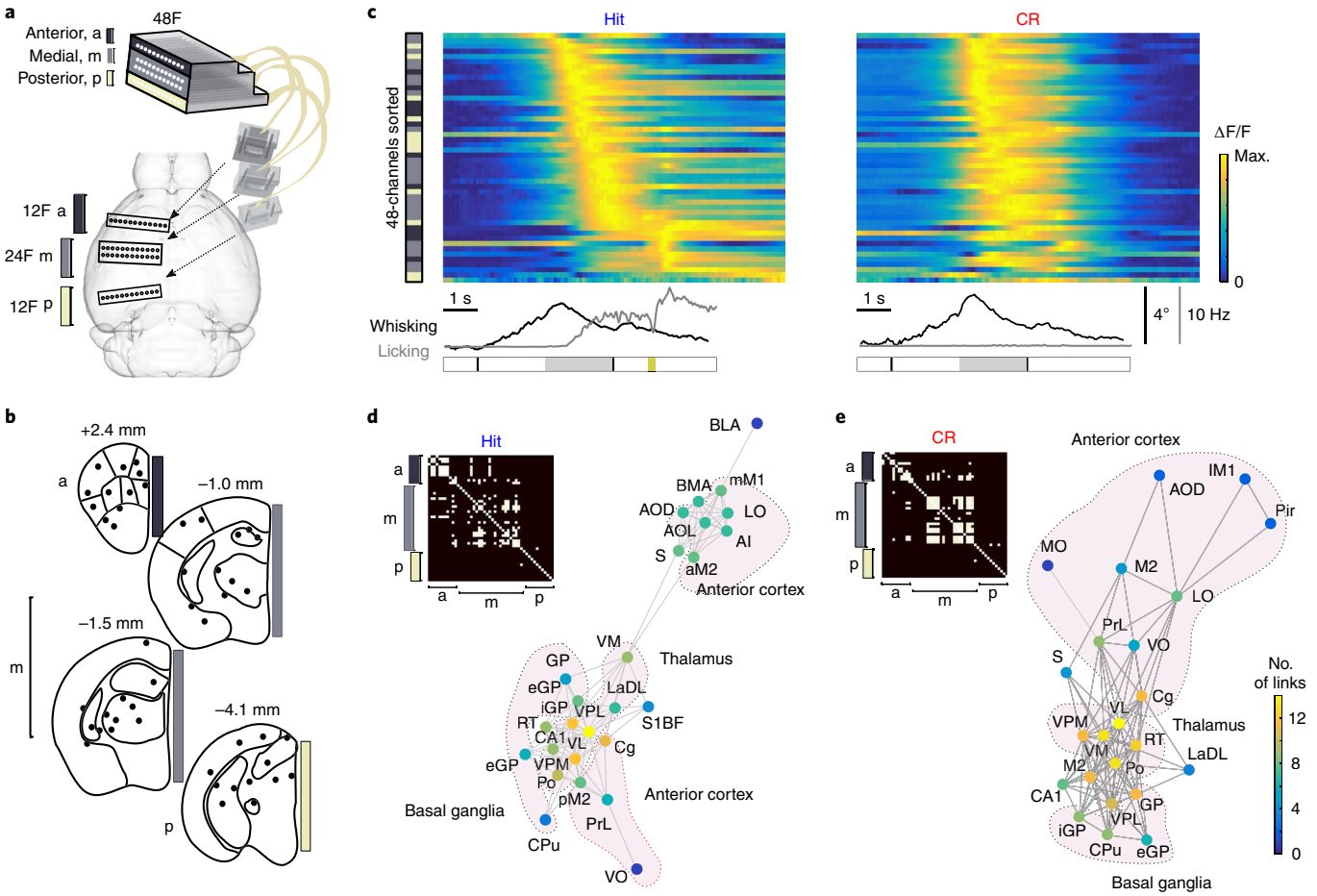

Fig. 3 | Simultaneous 48-channel multi-fiber photometry during texture discrimination. a, Top view of brain surface with implanted multi-fiber arrays (24-fiber array at 1.4 mm posterior bregma, including the same region targets as in 12-fiber experiments; two additional 12-fiber arrays, at 2.4 mm anterior and 4.1 mm posterior bregma, respectively). **b**, Schematic of fiber tips in an example 48-fiber experiment distributed across areas in anterior cortex (a), medial areas of the basal ganglia–thalamocortical loop (m) and visual-hippocampal areas in the posterior section (p). Numbers indicate rostrocaudal position relative to bregma. **c**, Heat maps of trial-averaged R-CaMP1.07 signals for Hit and CR trials. Average ΔF/F traces were normalized to their peak values. Traces are sorted according to the timing of 90% of their peak value. Left vector depicts the distribution of anterior, medial and posterior regions using the same color-coding as in **a**. Bottom: mean whisking envelope and mean licking rate for Hit and CR trials. Horizontal bar plot indicates trial structure according to Fig. 2a. **d**, Top left: the adjacency matrix computed with pairwise cross-correlation (correlation coefficients above shuffled mean + three standard deviations were included for respective Hit and CR trials). Functional network representation as in Fig. 2d reconstructed for Hit trials. Areas (nodes) are colored according to the number of links. **e**, Same plots as in **d** for CR trials. **c**–**e**, Number of trials: 224 for Hit, 210 for CR.

connected via links, and we visualized the resulting network with 'force-directed placement' separately for Hit and CR trials (Fig. 2d). Thalamic nuclei (VM, VL) and S1BF possessed more links than other areas, thus taking a central network position.

To demonstrate scaling up of multi-fiber photometry to even larger brain networks, we additionally implanted three mice with 48 fibers distributed across three front pieces implanted in one hemisphere (Fig. 3a). The three-fiber bundle branches converged at their proximal ends into a 48-fiber connector, coupling all channels to the photometry system. This approach allowed us to record calcium signals from a larger mesoscale network, now including additional areas in the anterior cortex (mostly anterior motor cortex and prefrontal areas) and posterior regions (visual cortex, ventral hippocampus and superior colliculus; Fig. 3b). Trial-averaged ΔF/F calcium signals (in this case, R-CaMP1.07) peaked during texture presentation in many regions (Fig. 3c; for examples of Hit and CR trials for all regions, see Supplementary Fig. 8 and Supplementary Video 1; comparison among all mice is shown in Supplementary Fig. 9). In addition, multiple cortical and subcortical areas displayed increased population responses following reward delivery. These preliminary observations indicate the recruitment of a distributed network during texture discrimination and demonstrate how high-density fiber arrays can scale up fiber photometry to brain-wide networks.

Quantification of functional connectivity by pairwise cross-correlations revealed 48-region functional networks for Hit and CR trials that formed several distinct clusters (anterior cortical areas, thalamus and basal ganglia) with features matching known anatomy (Fig. 3d,e and Supplementary Fig. 9). For example, the cluster of thalamic nuclei positioned between basal ganglia and anterior cortical areas reflects the anatomical organization of the basal ganglia–thalamocortical loop[30]. Specifically, VL and VM—known to project diffusely to multiple anterior cortical regions in addition to sensory cortices[29]—connected basal ganglia to the anterior cortex in the functional network. Multi-fiber photometry thus enables analysis of behavior-related functional connectivity patterns encompassing several tens of brain regions. Based on our network analysis, one can predict that perturbation of ventral thalamus (VM or VL) may strongly affect anterior cortical circuits, and this prediction can be tested by the combination of multi-fiber photometry with optogenetics through the same set of fibers.

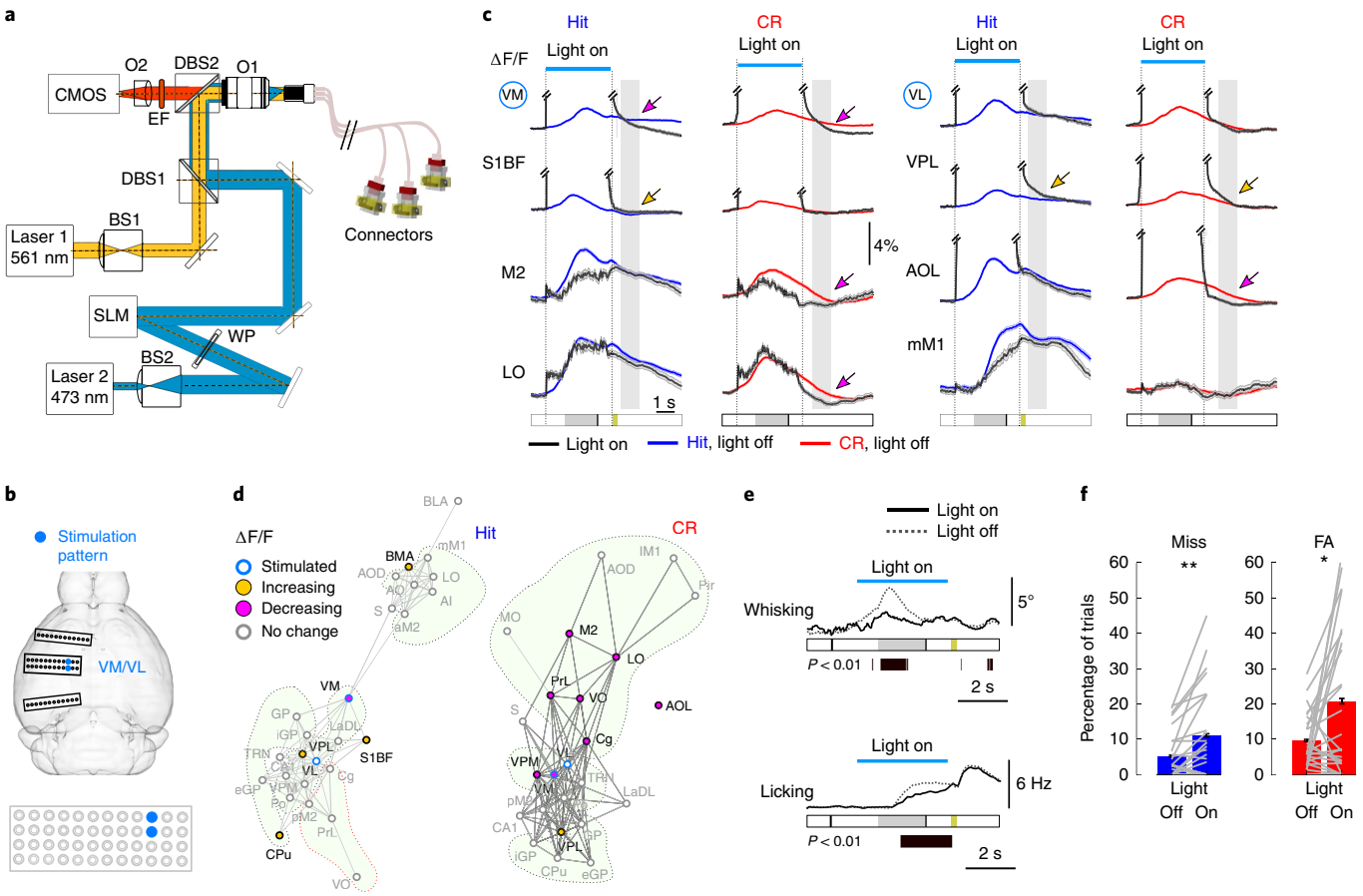

Fig. 4 | Combining multi-fiber photometry with optogenetic perturbation. a, Schematic of optical setup adapted for optogenetics. Laser 1 excites R-CaMP1.07, and laser 2 excites ChR2. Beam 2 is shaped with a 5× beam expander (BS2), a half-wave plate (WP) and the SLM to create the required beamlets in the focal plane of the objective (O1). Two dichroic beam splitters (DBS1/2) combine lasers for photometry and optogenetics and separate excitation and fluorescence emission, respectively. **b**, Position of the 48-fiber implants highlighting the VL and VM fiber channels targeted for optogenetic perturbation. **c**, Trial-averaged ΔF/F signals for example brain regions (mean ± s.e.m.). Black traces, perturbed trials ('Light on'); blue, unperturbed Hit trials; red, unperturbed CR trials. Arrows highlight examples of significant divergence ($P < 0.05$; one-way ANOVA) of perturbed and unperturbed ΔF/F signals in the time window for post-perturbation analysis (gray vertical bar). The perturbed areas in VL and VM are circled. **d**, Impact of VM and VL perturbation on functional network representation for Hit (left) and CR (right) trials (networks in gray taken from Fig. 3d,e). Magenta, regions showing decrease in ΔF/F signal in the analysis time window ($P < 0.05$; one-way ANOVA); yellow, regions with increased ΔF/F ($P < 0.05$; one-way ANOVA); blue circles, perturbed regions; gray circles, unaffected regions. **e**, Reduction in whisking and licking rates following VM and VL perturbation (solid and dashed lines from perturbed and unperturbed trials, respectively; black bars, periods of significant difference in whisking and licking; $P < 0.01$, one-way ANOVA). **c**–**e**, Data from one example session with 58 and 244 perturbed and unperturbed Hit trials and 44 and 210 perturbed and unperturbed CR trials, respectively. **f**, Increase in Miss (blue) and False Alarm (FA, red) rates following optogenetic perturbation in VM and/or VL (mean ± s.e.m.; 23 sessions, four mice, two-sided Wilcoxon signed-rank test; $^{*}P = 0.0199$, $z = 2.32$ for FA and $^{**}P = 0.0019$, $z = 3.10$ for Miss trials).

Combining multi-fiber photometry with optogenetic perturbation. To demonstrate that multi-fiber photometry can be combined with targeted optogenetic perturbations, we used a spatial light modulator (SLM) in a second laser beam path, creating multiple beamlets for coupling into a selected subset of fiber channels (Fig. 4a,b). Thereby, either individual or multiple regions can be targeted for optogenetic perturbation. In VGAT-ChR2 EYFP transgenic mice, in which local neural circuits can be inhibited by blue-light excitation of ChR2-expressing GABAergic interneurons, we virally expressed R-CaMP1.07 in the brain regions targeted by the multi-fiber array ($n = 3$ mice; one 48-fiber implant and two 12-fiber implants). Our goal was to perturb part of the functional brain network during texture discrimination behavior to induce changes in network dynamics and possibly behavior.

With the SLM, we created a beamlet pattern to target, either in combination or separately (Fig. 4b), VL and VM, the central nodes in the functional network whose activity also strongly correlated with behavioral variables (Fig. 2e). However, because GABAergic neurons in the thalamus are sparse and because VL and VM also receive GABAergic axonal projections from elsewhere (for example, RT and GP), optogenetic stimulation may have multiple effects, including antidromic activation of adjacent regions. We verified this possibility in control mice with electrical recordings and indeed found non-local activation of neurons in RT, but could also confirm decreased neuronal activation in the targeted thalamic area (Supplementary Fig. 10).

How does perturbation of a subset of regions affect the larger functional network? We perturbed VL and VM during behavior in a random 30% of trials for a 4-s period starting before first whisker–texture touch and lasting until 1 s after texture withdrawal (Fig. 4c). Because of stimulation artifacts that occurred during and shortly after the stimulation period (Supplementary Notes), we restricted our analysis of mean ΔF/F signal changes to a time window of 0.5–1.5 s after the perturbation laser was turned off. In this analysis

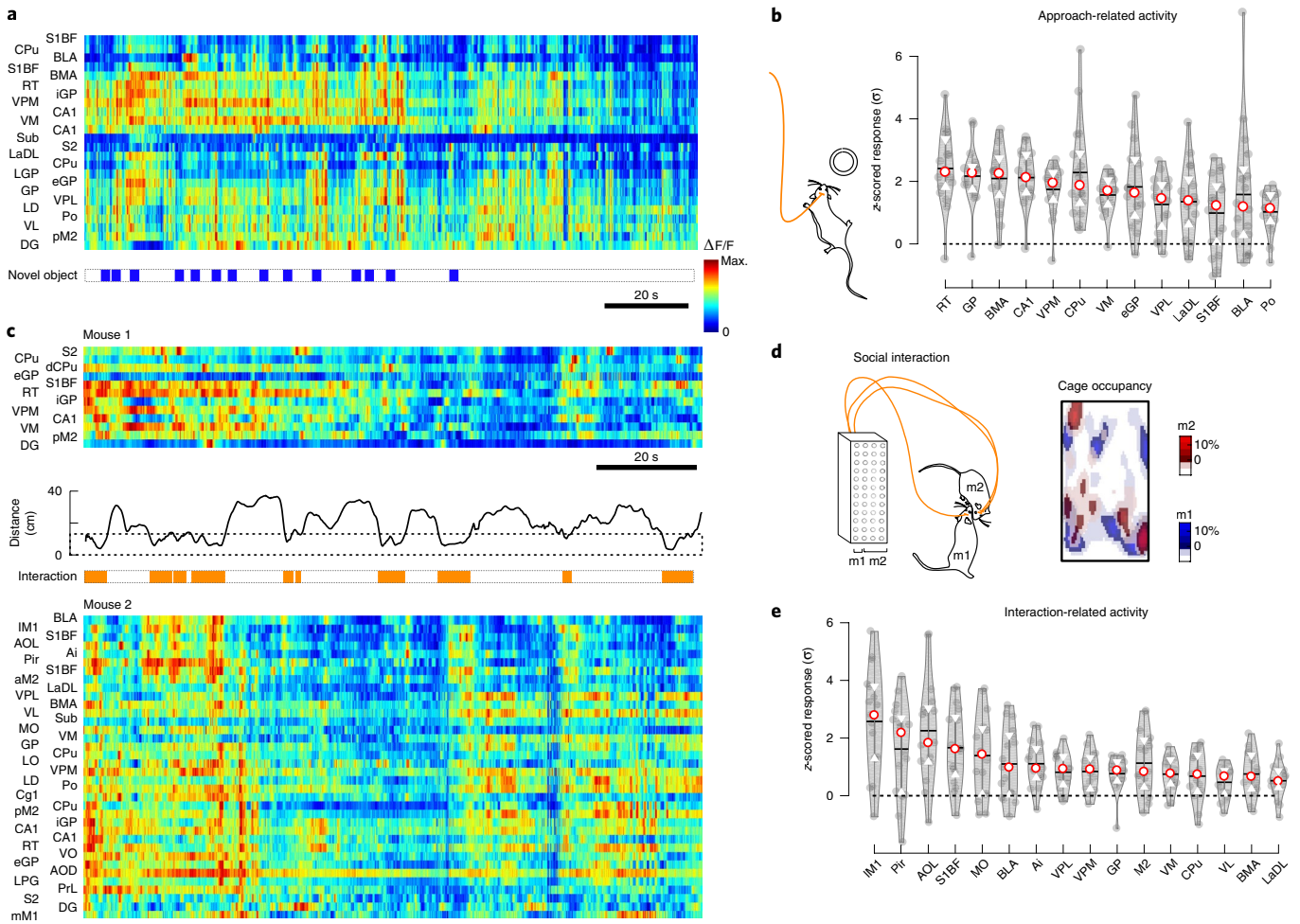

Fig. 5 | Multi-fiber photometry in freely moving mice. a, Multi-fiber photometry in a mouse freely exploring a cage with a novel object. Bottom: blue bars mark time periods of object approach (<20-cm distance). **b**, Regions displaying significant changes in *z*-scored ΔF/F following approach toward the novel object. **c**, Simultaneous fluorescence recording in 48 channels from two socially interacting mice (mouse 1, 12 fibers; mouse 2, 36 fibers). **d**, Left: schematic interaction of the pair of mice. Right: cage occupancy (mouse 1 (m1) in blue and mouse 2 (m2) in red). **e**, Regions displaying significant changes in *z*-scored ΔF/F for time periods when mice were approaching each other. **b**,**e**, Distribution plots showing median (red circles), mean (black lines) and 25th and 75th percentiles (bottom and top white notches). Fluorescence responses from 18 approaches to a novel object and 17 social interaction events (3-s periods following approach) were *z*-scored according to mean and standard deviation of the ΔF/F signal for time periods when the object or companion mouse was far away (>20 cm). We used two-sided Wilcoxon signed-rank test to determine whether the distribution of approach- or interaction-related activity was different from that with median at zero (only regions with $P < 0.01$ are shown).

window (after VM and VL perturbation), we observed for both Hit and CR trials a significant reduction of the ΔF/F signal in VM and a decrease, though not significant, in VL ($P < 0.05$, one-way ANOVA; Fig. 4c,d). In addition, several other regions were affected. For example, in line with our prediction above, several anterior cortical areas showed significantly reduced activity after thalamic perturbation in CR trials ($P < 0.05$, one-way ANOVA). Further signal changes occurred in S1BF and CA1 following individual perturbations of VM or VL (Supplementary Fig. 12). As all experimental parameters were identical in Hit and CR trials, the differential network effects suggest that optogenetic perturbation caused trial-type-dependent changes in mesoscale circuit dynamics. While these results are preliminary, the main purpose of the experiments was to demonstrate the feasibility of combining multi-fiber photometry with optogenetics.

Do thalamic perturbations also affect behavior? Indeed, whisking and licking were significantly reduced ($P < 0.01$, one-way ANOVA; Fig. 4e and Supplementary Fig. 12), which is consistent with the strong correlation of VM and VL calcium signals with these variables (Fig. 2d). Furthermore, all mice showed increased rates of Misses and False Alarms following thalamic perturbation (Fig. 4f). More False Alarm trials with incorrect licking indicate that impairment in behavioral performance is not simply due to suppressed motor function. Thus, optogenetic manipulations through high-density fiber arrays are feasible in combination with multi-fiber photometry. Therefore, one can first identify relevant active regions in the mesoscale network and then specifically study how perturbation of these regions affects functional connectivity, network dynamics and behavior.

Multi-fiber photometry in freely moving mice. The lightweight fiber bundles and miniaturized fiber arrays also facilitate experiments in freely moving animals. As proof of concept, we applied multi-fiber photometry to mice freely exploring an environment with a novel object. In several brain regions—including particularly RT, GP and BMA—we observed ΔF/F changes related to object approach (Fig. 5a,b). We also explored multi-fiber photometry application in two interacting mice. We connected separate

branches of a fiber bundle to two male mice (one with a 12-fiber implant, the other with a 36-fiber implant), which were placed in the same cage and approached each other multiple times during a session (Fig. 5c,d and Supplementary Video 2). Several regions in both mice showed activation during these social encounters, including cortical regions (lM1, S1BF), olfactory regions (Pir, AOL) and amygdala (BLA), among others (Fig. 5e). Consistent with recent studies[31], it is likely that BLA and BMA neuronal ensembles encode context-specific information relevant for social interaction while other areas such as S1BF and Pir may reflect multiple aspects of social touch and olfactory processing initiated by social interaction. Although more quantitative parametrization of behavioral variables will be required, multi-fiber photometry in freely moving animals thus offers exciting new options to advance our understanding of long-range circuits underlying complex naturalistic behaviors, including social interactions.

Discussion

Multi-fiber arrays complement existing neural interfaces for readout and optical control of large-scale network dynamics in the mammalian brain. We scaled up photometry recordings to 48 brain regions, combined the multi-fiber photometry with optogenetic perturbations and demonstrated applications in both head-fixed and freely moving mice. While these results highlight the versatility of multi-fiber arrays, in the following we discuss further prospects in terms of technology and applications.

We believe that the number of fiber channels can be further increased. Because of their compactness and low weight, even implantation of six front pieces into a rodent brain seems feasible, particularly if they are distributed across hemispheres, and possibly the cerebellum too. If each front piece carries 24 fibers, this approach could enable simultaneous recording from 100–150 regions. As tissue tolerates the fibers well, brain damage associated with multi-fiber implants might be kept at a bearable level. For example, compared to a 3-mm cannula window above CA1—a common method for hippocampal imaging requiring tissue aspiration[32]—the total volume of inserted fiber material in our 48-channel experiment was around fivefold smaller (~1.2 mm^3 compared to ~7.7 mm^3). Thinner optical fibers or tapered fiber tips[33] could render fiber probes even less invasive. To maximize the number of simultaneously imaged regions, one could integrate multi-fiber arrays into wide-field microscopes[12–15]—for example, by implanting fiber arrays at an angle. Two cameras, or dedicated segments of the same CMOS sensor, would measure multi-fiber and wide-field signals in parallel. Further hybrid approaches may combine multi-fiber arrays with other existing technologies. For example, high-density fiber arrays could expand the use of fiber optics in fMRI experiments[34–36] and help to improve understanding of the relationships among neuronal, glial and vascular dynamics. Through combination with extracellular silicon probes[6] or emerging optoelectronic neural probes[37,38], the activity of individual neurons could be related to larger-scale population activity[39], even up to the mesoscale[40]. Similarly, in combination with multi-site neurochemical recordings[41], this would allow studies of how neuromodulator activity impacts brain-wide neural network dynamics.

Multi-fiber arrays are especially well suited for applications in behaving animals, both head-fixed and freely moving. Multi-fiber photometry should be equally well applicable in mice, rats, non-human primates[42] and other mammalian species. As with single-fiber approaches[19,21], multi-fiber approaches will gain their full strength through combination with genetic tools for cell-type- or pathway-specific labeling with optical indicators (for neuronal calcium levels, voltage[20], dopamine release[43], glial dynamics[35,36], metabolic substrates[44] and so on). In addition to pathway-specific labeling, nuclear expression of calcium indicators could circumvent ambiguities in signal assignment and dissect mixed components in fiber-optic bulk signals. Likewise, multi-fiber implants could be useful in photo-activation experiments employing calcium integrators for marking or targeting neuronal subpopulations that were activated during specific time windows[45,46]. Multi-color approaches should allow parallel usage of multiple indicator systems. Finally, as demonstrated here in VGAT-ChR2 mice, multi-fiber arrays can also be applied for multi-site optogenetic control, benefitting from the large available palette of opsins[47] and photo-activatable molecules. Various combinations of activity reporters with optogenetic actuators exist. Suitable expression of the respective proteins throughout the brain may be achieved by supplementary viral injections in transgenic mouse lines[48]. Virus release from silk fibroin drops[49] applied to the fiber tips could alleviate the workload of multiple virus injections and facilitate more complex expression patterns. Integration of optogenetic manipulations with multi-fiber photometry or wide-field imaging[12] should enable all-optical studies on the mesoscale, complementing current efforts to establish all-optical interrogation at the microcircuit level with single-cell precision[50].

We anticipate that multi-fiber arrays will become important tools for studying the complex functional organization of the mammalian forebrain. Not only do they allow the reconstruction of functional networks related to specific behaviors, but they also can be applied longitudinally to study network changes over long time spans—for example, during learning or disease progression. Also, with the help of more sophisticated network analysis methods, multi-fiber photometry data should thus facilitate unbiased functional mapping of brain networks to identify circuit components relevant under various conditions of both health and disease.

Online content

Any methods, additional references, Nature Research reporting summaries, source data, statements of code and data availability, and associated accession codes are available at https://doi.org/10.1038/s41592-019-0400-4.

Received: 14 August 2018; Accepted: 28 March 2019;
Published online: 13 May 2019

References

1. Prevedel, R. et al. Simultaneous whole-animal 3D-imaging of neuronal activity using light-field microscopy. *Nat. Methods* **11**, 727–730 (2014).
2. Mann, K., Gallen, C. L. & Clandinin, T. R. Whole-brain calcium imaging reveals an intrinsic functional network in *Drosophila*. *Curr. Biol.* **27**, 2389–2396 (2017).
3. Keller, P. J. & Ahrens, M. B. Visualizing whole-brain activity and development at the single-cell level using light-sheet microscopy. *Neuron* **85**, 462–483 (2015).
4. Mace, E. et al. Functional ultrasound imaging of the brain. *Nat. Methods* **8**, 662–664 (2011).
5. Siegel, M., Buschman, T. J. & Miller, E. K. Cortical information flow during flexible sensorimotor decisions. *Science* **348**, 1352–1355 (2015).
6. Jun, J. J. et al. Fully integrated silicon probes for high-density recording of neural activity. *Nature* **551**, 232–236 (2017).
7. Luo, L., Callaway, E. M. & Svoboda, K. Genetic dissection of neural circuits: a decade of progress. *Neuron* **98**, 256–281 (2018).
8. Lecoq, J. et al. Visualizing mammalian brain area interactions by dual-axis two-photon calcium imaging. *Nat. Neurosci.* **17**, 1825–1829 (2014).
9. Chen, J. L., Voigt, F. F., Javadzadeh, M., Krueppel, R. & Helmchen, F. Long-range population dynamics of anatomically defined neocortical networks. *eLife* **5**, e14679 (2016).
10. Stirman, J. N., Smith, I. T., Kudenov, M. W. & Smith, S. L. Wide field-of-view, multi-region, two-photon imaging of neuronal activity in the mammalian brain. *Nat. Biotechnol.* **34**, 857–862 (2016).
11. Sofroniew, N. J., Flickinger, D., King, J. & Svoboda, K. A large field of view two-photon mesoscope with subcellular resolution for in vivo imaging. *eLife* **5**, e14472 (2016).
12. Lim, D. H. et al. In vivo large-scale cortical mapping using channelrhodopsin-2 stimulation in transgenic mice reveals asymmetric and reciprocal relationships between cortical areas. *Front. Neural Circuits* **6**, 11 (2012).

13. Allen, W. E. et al. Global representations of goal-directed behavior in distinct cell types of mouse neocortex. *Neuron* **94**, 891–907 (2017).
14. Chen, T. W., Li, N., Daie, K. & Svoboda, K. A map of anticipatory activity in mouse motor cortex. *Neuron* **94**, 866–879 (2017).
15. Gilad, A., Gallero-Salas, Y., Groos, D. & Helmchen, F. Behavioral strategy determines frontal or posterior location of short-term memory in neocortex. *Neuron* **99**, 814–828 (2018).
16. Ghosh, K. K. et al. Miniaturized integration of a fluorescence microscope. *Nat. Methods* **8**, 871–878 (2011).
17. Adelsberger, H., Garaschuk, O. & Konnerth, A. Cortical calcium waves in resting newborn mice. *Nat. Neurosci.* **8**, 988–990 (2005).
18. Lütcke, H. et al. Optical recording of neuronal activity with a genetically-encoded calcium indicator in anesthetized and freely moving mice. *Front. Neural Circuits* **4**, 9 (2010).
19. Cui, G. et al. Concurrent activation of striatal direct and indirect pathways during action initiation. *Nature* **494**, 238–242 (2013).
20. Marshall, J. D. et al. Cell-type-specific optical recording of membrane voltage dynamics in freely moving mice. *Cell* **167**, 1650–1662 (2016).
21. Gunaydin, L. A. et al. Natural neural projection dynamics underlying social behavior. *Cell* **157**, 1535–1551 (2014).
22. Anikeeva, P. et al. Optetrode: a multichannel readout for optogenetic control in freely moving mice. *Nat. Neurosci.* **15**, 163–170 (2012).
23. Warden, M. R., Cardin, J. A. & Deisseroth, K. Optical neural interfaces. *Annu. Rev. Biomed. Eng.* **16**, 103–129 (2014).
24. Kim, C. K. et al. Simultaneous fast measurement of circuit dynamics at multiple sites across the mammalian brain. *Nat. Methods* **13**, 325–328 (2016).
25. Guo, Q. et al. Multi-channel fiber photometry for population neuronal activity recording. *Biomed. Opt. Express* **6**, 3919–3931 (2015).
26. Joel, D. & Weiner, I. The organization of the basal ganglia-thalamocortical circuits: open interconnected rather than closed segregated. *Neuroscience* **63**, 363–379 (1994).
27. Zeng, H. Mesoscale connectomics. *Curr. Opin. Neurobiol.* **50**, 154–162 (2018).
28. Chen, J. L., Carta, S., Soldado-Magraner, J., Schneider, B. L. & Helmchen, F. Behaviour-dependent recruitment of long-range projection neurons in somatosensory cortex. *Nature* **499**, 336–340 (2013).
29. Collins, D. P., Anastasiades, P. G., Marlin, J. J. & Carter, A. G. Reciprocal circuits linking the prefrontal cortex with dorsal and ventral thalamic nuclei. *Neuron* **98**, 366–379 (2018).
30. Oh, S. W. et al. A mesoscale connectome of the mouse brain. *Nature* **508**, 207–214 (2014).
31. Kim, Y. et al. Mapping social behavior-induced brain activation at cellular resolution in the mouse. *Cell Rep.* **10**, 292–305 (2015).
32. Pilz, G.-A. et al. Functional imaging of dentate granule cells in the adult mouse hippocampus. *J. Neurosci.* **36**, 7407–7414 (2016).
33. Pisanello, F. et al. Dynamic illumination of spatially restricted or large brain volumes via a single tapered optical fiber. *Nat. Neurosci.* **20**, 1180–1188 (2017).
34. Lee, J. H. et al. Global and local fMRI signals driven by neurons defined optogenetically by type and wiring. *Nature* **465**, 788–792 (2010).
35. Schulz, K. et al. Simultaneous BOLD fMRI and fiber-optic calcium recording in rat neocortex. *Nat. Methods* **9**, 597–602 (2012).
36. Schlegel, F. et al. Fiber-optic implant for simultaneous fluorescence-based calcium recordings and BOLD fMRI in mice. *Nat. Protoc.* **13**, 840–855 (2018).
37. Wu, F. et al. Monolithically integrated μLEDs on silicon neural probes for high-resolution optogenetic studies in behaving animals. *Neuron* **88**, 1136–1148 (2015).
38. Lu, L. et al. Wireless optoelectronic photometers for monitoring neuronal dynamics in the deep brain. *Proc. Natl. Acad. Sci. USA* **115**, 1374–1383 (2018).
39. Okun, M. et al. Diverse coupling of neurons to populations in sensory cortex. *Nature* **521**, 511–515 (2015).
40. Xiao, D. et al. Mapping cortical mesoscopic networks of single spiking cortical or sub-cortical neurons. *eLife* **6**, e19976 (2017).
41. Schwerdt, H. N. et al. Subcellular probes for neurochemical recording from multiple brain sites. *Lab Chip* **17**, 1104–1115 (2017).
42. Adelsberger, H., Zainos, A., Alvarez, M., Romo, R. & Konnerth, A. Local domains of motor cortical activity revealed by fiber-optic calcium recordings in behaving nonhuman primates. *Proc. Natl. Acad. Sci. USA* **111**, 463–468 (2014).
43. Patriarchi, T. et al. Ultrafast neuronal imaging of dopamine dynamics with designed genetically encoded sensors. *Science* **360**, eaat4422 (2018).
44. Mächler, P. et al. In vivo evidence for a lactate gradient from astrocytes to neurons. *Cell Metab.* **23**, 94–102 (2016).
45. Fosque, B. F. et al. Neural circuits. Labeling of active neural circuits in vivo with designed calcium integrators. *Science* **347**, 755–760 (2015).
46. Lee, D., Hyun, J. H., Jung, K., Hannan, P. & Kwon, H.-B. A calcium- and light-gated switch to induce gene expression in activated neurons. *Nat. Biotechnol.* **35**, 858–863 (2017).
47. Chuong, A. S. et al. Noninvasive optical inhibition with a red-shifted microbial rhodopsin. *Nat. Neurosci.* **17**, 1123–1129 (2014).
48. Madisen, L. et al. Transgenic mice for intersectional targeting of neural sensors and effectors with high specificity and performance. *Neuron* **85**, 942–958 (2015).
49. Jackman, S. L. et al. Silk fibroin films facilitate single-step targeted expression of optogenetic proteins. *Cell Rep.* **22**, 3351–3361 (2018).
50. Chen, I.-W., Papagiakoumou, E. & Emiliani, V. Towards circuit optogenetics. *Curr. Opin. Neurobiol.* **50**, 179–189 (2018).

Acknowledgements

We would like to thank H. Kasper, M. Wieckhorst and S. Giger for technical assistance; J. L. Alatorre Warren for the registration of histology sections to the Allen Brain Atlas and fiber shaft tracking; A. Jovalekic for help with electrophysiological recordings and spike sorting; and A. Ayaz, L. Egolf and C. Lewis for comments on the manuscript. This work was supported by grants to F.H. from the Swiss National Science Foundation (No. 310030B_170269) and the European Research Council (ERC Advanced Grant, project No. 670757, BRAINCOMPATH), by a Transfer Project and an IPhD Project from SystemsX.ch (Nos. 51TP-0_145729 and 51PHP0_157359, respectively) and through a Roche Joint Collaborative Project.

Author contributions

Y.S. and F.H. designed the experiments. Y.S. conducted the experiments and analyzed the data. M.C. assisted in fiber-optic experiments. L.S. performed brain histology. Y.S. and F.H. wrote the paper.

Competing interests

The authors declare no competing interests.

Additional information

Supplementary information is available for this paper at https://doi.org/10.1038/s41592-019-0400-4.

Reprints and permissions information is available at www.nature.com/reprints.

Correspondence and requests for materials should be addressed to Y.S. or F.H.

Publisher's note: Springer Nature remains neutral with regard to jurisdictional claims in published maps and institutional affiliations.

Methods

Design of high-density, multi-fiber arrays. Step-by-step construction of a multi-fiber array is illustrated in Supplementary Fig. 2. We utilized components of fiber connector technology, specifically, ferrules that can accommodate various numbers of fibers (8, 12, 24 and 48 fibers; Nos. 17185, 7413, 12599, US Conec). Optical fibers with polyimide coating (100-µm core diameter, 124-µm outer diameter, 0.22-NA, No. UM22-100, Thorlabs) were fitted into the ferrule. For targeting of specific subsets of brain regions, fibers were aligned to templates defining the required implantation depths. After alignment, we glued fibers inside the ferrule with a two-component epoxy (302-3M 1LB Kit Parts A and B, Epoxy Technology). An additional drop of epoxy was applied to the surface connecting to the fiber bundle. After letting the epoxy cure for 24 h, we polished the surface in consecutive steps starting with a rough diamond lapping sheet (30-µm grit), then changing to a silicon carbide lapping sheet (5-µm grit) and gradually moving to a calcined alumina lapping sheet of 0.3-µm grit (Nos. LF30D, LF5P, LF3P and LF1P–03P, Thorlabs). A custom-designed bare-ferrule polishing puck held the ferrule orthogonal to the polishing pad (No. NRS913A, Thorlabs). Ethanol applied to the polishing pad reduced friction. After polishing, we added alignment pins (Nos. 16741 and 16742, US Conec). A custom-designed magnetic housing was attached after fixation of the multi-fiber array to the skull with dental cement. Coupling efficiency between a 12-fiber implant and the connecting bundle was 75.2% ± 1.2% (mean ± s.e.m.).

Design of fiber bundles connecting to multi-fiber implants. Fiber bundles connecting multi-fiber implants to the fiber photometry setup were designed similarly to multi-fiber array front pieces. First, optical fibers (No. UM22-100, 0.22-NA, 100-µm core, Thorlabs) were cut to the required length with a ruby fiber scribe (No. S90R, Thorlabs). For head-fixed texture discrimination behavior, we used 2-m-long fiber bundles. For free movement experiments, we prepared a 3-m-long bundle. To protect fibers, we fitted four fibers each into protective light weight tubing (No. FT900Y, Thorlabs). After positioning all fibers, we applied epoxy to the ferrules and an extra drop to stabilize the fiber facet for subsequent polishing, thus ensuring high-quality optical coupling between multi-fiber implant and fiber bundle. Both proximal and distal ends of the fiber bundle were polished as described above. The proximal fiber connector was mounted in a custom-designed holder fitted into a 30-mm cage XY-translator for 1-inch-diameter optics (No. CXY1, Thorlabs) for positioning in the optical setup.

Optical setup. The proximal end of the fiber bundle was integrated into the photometry setup for calcium recordings and optogenetic manipulations. We used an Omicron LuxX 473-nm laser (or, alternatively, a Coherent OBIS LX 488-nm laser) for excitation of virally expressed GCaMP6m and activation of ChR2, and a Coherent OBIS LS 561-nm laser to excite R-CaMP1.07. Lasers were run at 80% maximal output power for stable continuous wave operation. A variable neutral density filter (No. NDC-25C-4M, Thorlabs) reduced fluorescence excitation power to ~1.3 mW mm^{-2} at each fiber tip. Cylindrical lenses were used to create appropriate illumination patterns at the object plane of the objective. First, an achromatic Galilean beam expander (No. GBE05-A, Thorlabs) expanded and collimated the circular beam. Second, a line illumination pattern matching the 12-fiber array was created with a 75-mm focal length cylindrical lens (No. LJ1703RM-A, Thorlabs) placed ~145 mm from the objective (No. TL4x-SAP, Thorlabs). For the 48-fiber array, we created a rectangular illumination pattern by adding a 150-mm focal length cylindrical lens (No. LJ1629RM-A, Thorlabs) oriented 90° to the first cylindrical lens. A first dichroic beam-splitter (No. F38-495, AHF) combined the two laser beams along the optical axis. A second dichroic beam-splitter (No. F58-486 dual line, AHF) coupled excitation light into the objective (No. TL4x-SAP, Thorlabs) and transmitted fluorescence signals for both GCaMP6m and R-CaMP1.07. Residual excitation light and broad-spectrum auto-fluorescence were suppressed with emission filters (525/50 nm, No. F37-516, AHF, for GCaMP6m and 605/70 nm, No. F47-605, for R-CaMP1.07) and multi-line notch filters from Chroma Technology Corp. (No. ZET405/473/561 and a combination of ZET405/488 and ZET488/561, respectively). The fiber array end face was imaged onto the camera sensor (ORCA Flash4.0, Hamamatsu camera) with a tube lens with internal focusing (Proximity Series InfiniTube, 200-mm focal length).

Animals and surgical procedures. All animal experiments were carried out according to the guidelines of the Veterinary Office of Switzerland and approved by the Cantonal Veterinary Office in Zurich. A total of 32 male mice (age 2–6 months) were used in this study. GCaMP6m expression[51,52] was induced by injection of AAV2.9-hSyn-GCaMP6m into the brains of C57BL/6 mice (n = 18), and a 12-fiber array was subsequently implanted. Mice were anesthetized with 2% isoflurane (in pure oxygen). Body temperature was maintained at 37 °C. To prevent inflammation and pain during anesthesia, we injected 0.1 µl/g body weight meloxicam subcutaneously. Connective tissue was removed from the skull, which was additionally polished and dried. To ensure optimal adhesion of the skull to the connective dental cement, we applied iBond (Kulzer, Total Etch). To further stabilize the implant, we used a thin ring of Charisma (Kulzer, A1) on the skull rim. Both iBond and Charisma were ultraviolet-cured. Small, slit-like craniotomies were made to allow for virus injections and implantation of fiber arrays (carried out on the same day). First, ~120 nl of AAV2.9-hSyn-GCaMP6m were pressure-injected at 20 nl min^{-1} through glass pipettes (diameter: 10–15 µm) into all regions of interest (using a syringe and pressure control with a barometer). To allow local diffusion and avoid possible refluxes, we kept the pipettes in place for 10 min after injection. Twelve-fiber arrays were implanted +0.4 mm from the midline, tilted at an angle of 15°. We oriented the fiber array such that the most lateral fiber efficiently targeted CPu (−1.06 mm from bregma) and the most medial fiber targeted hippocampal areas (CA1, DG; −1.46 mm). Before fiber implantation, we slightly scratched the dura surface. The craniotomy was sealed with Vaseline, which melts at body temperature and completely covered the craniotomy. Next, we applied dental cement (Tetric EvoFlow, A1) on the skull and around the implant followed by ultraviolet-light curing. A lightweight metal head post was cemented to the skull, allowing for head-fixation during the behavioral experiments. After 2 weeks of recovery, mice were habituated to head-fixation and trained in the texture discrimination task. For the six mice with 12-fiber implants, we performed fiber-optic recordings over 25 ± 10 d (mean ± s.d., minimum 16 d and maximum 43 d, depending on individual learning rates). The goal of these behavioral experiments was to record for 2 weeks after a mouse reached expert performance level. Thereafter, the experiment was considered successful and terminated, not because of a failure of the implant. We attempted 12-fiber implantation in a total of 18 animals; our overall success rate thus was 33%. We encountered failures of several kinds, some due to our inexperience. Hence, it is hard to pinpoint and systematically address only one or a few types of failure. Given the various initial adjustments that we made to optimize indicator expression, histology and so on, we believe that a success rate for multi-fiber implants of >60% should be possible once the protocol is fully established. Homogeneity and expression levels of fluorescent indicators could be further improved by the use of transgenic mouse lines[48].

Transgenic VGAT-ChR2-EYFP mice[53] (n = 7) were injected with AAV2.1-EF1a-R-CaMP1.07 and implanted with multi-fiber arrays as described above. Four mice were implanted with single 12-fiber arrays. Three mice received three array implants: two arrays with 12 fibers each plus one with 24 (total, 48 channels). Here, the single 12-fiber arrays were implanted in the frontal and posterior regions (+2.4 and −4.1 mm from bregma, respectively), whereas the 24-fiber array targeted the same regions as in the 12-fiber array experiments (implanted at −1.46 mm), with additional fibers implanted in the ventral striatum (vCPu), lateral globus pallidus (LGP), lateral thalamus (Po and VPL) and amygdala nuclei (BMA, BLA and LaDL).

Two VGAT-ChR2-EYFP mice were used for electrophysiological characterization of optogenetic perturbation effects in VL and RT. To combine fiber photometry and extracellular electrophysiology, we implanted an opto-tetrode in each of two C57BL/6 mice, using a preparation protocol similar to that for the multi-fiber array. Mice were injected in the posterior M1 with 120 nl of AAV2.9-hSyn-GCaMP6m. The opto-tetrode was implanted at a depth of around 350 µm in the posterior M1, and a ground screw was placed contralateral to the implant hemisphere (see Supplementary Notes for further details). To evaluate the immune response induced by multi-fiber arrays, we implanted one transgenic CX3CR1–EGFP mouse with an array containing four UM22-100 optical fibers. Similarly, one C57BL/6 mouse was used for simultaneous histological staining of astrocytes (GFAP) and microglia (Iba1; see below and Supplementary Fig. 1). To estimate R-CaMP1.07 fluorescence and potential photo-activation with 473-nm excitation light (as used for optogenetic perturbation), we injected AAV2.1-EF1a-R-CaMP1.07 into one C57BL/6 mouse in the same set of medial regions as in the 12-fiber experiments.

Texture discrimination task. Following fiber array implantation and 2 weeks of recovery, mice were accommodated to head-fixation through a series of short-duration head-fixations. After commencement of water scheduling, each mouse was first trained to lick following texture presentation. After this shaping period, we presented either the go texture (P100 sandpaper) or no-go texture (P1200) and trained the mouse to discriminate the two texture types[28]. For the go texture, the mouse had to lick at a water spout to receive a water droplet as a reward (Hit trial). Failure to lick was considered as a Miss trial. For the no-go texture, the mouse had to refrain from licking (CR). Wrong licks resulted in False Alarms. Texture types were presented with 50% probability. Each trial started with a transistor–transistor logic (TTL) pulse synchronizing the fluorescence measurements with the behavioral setup. One second after commencement of the trial, a 2-kHz auditory tone (two 100-ms pulses at an interval of 50 ms) signaled the start of the texture approach (~90° to the whisker pad). The texture reached its end position after 2 s, but the first whisker-to-texture touch typically occurred shortly before when the texture came into reach of whiskers. The texture stayed in contact for 2 s and was retracted afterward, indicated by a second 4-kHz auditory tone (four 50-ms pulses at 25-ms interval). Water reward was delivered in Hit trials, with the valve opening for 6 s. A loud white-noise sound of 4-s duration was presented as punishment in False Alarm trials. Neither reward nor punishment was given in CR and Miss trials. The lick detector was reachable throughout the entire session. Textures were presented pseudo-randomly with no more than three consecutive presentations of the same texture type. Expert mice typically reported their decision by starting to lick during the later period of a texture presentation (3.5–4.0 s after start of trial) and then during the report period (5–7 s after trial start).

Novel object and social interaction assays. Mice were habituated for at least 2 weeks by the experimenter to the experimental room. For freely moving behavior, a type-T2L individually ventilated cage was placed below the optical setup at the floor level, with fiber bundles suspended from a support lever above the cage center releasing some of the bundle's weight off the animal's head. For each experiment, we used the cage anew with clean bedding. Room lighting was at daylight level. For novel object exploration, a single mouse was placed in the cage. After 1 min of free exploration, a novel object (black or blue plastic cylinder) was placed at the cage center. For the social interaction assay, a second mouse was placed at the opposite side to allow for a gradual approach (both mice were male). Sessions typically lasted 5 min. If a fiber bundle became too tangled, we disconnected and disentangled it by rotating it by hand in the opposite direction.

Optogenetic manipulation. The 473-nm laser was used to excite GABAergic neurons in VGAT-ChR2 EYFP transgenic mice. The beam was 5× expanded (No. GBE05-A, Thorlabs) and directed onto a spatial light modulator (SLM, No. SN 4479, Meadowlark Optics) to shape the wave front of the laser beam for patterned illumination. For a pure voltage-dependent phase shift, the linear polarization of the incident laser beam should be aligned parallel to the extraordinary axis of the SLM pixels, which we achieved with a zero-order half-wave plate (No. WPH10M-473, Thorlabs). One can then create a programmable phase-shift pattern by changing the voltage on the corresponding pixels. The phase-shift pattern across the SLM was optimized with the Gerchberg–Saxton algorithm to generate multiple beamlets in the object plane of the objective for parallel coupling of excitation light into the fiber channels selected for brain region perturbation. We applied a 4-s-long stimulation at 473 nm for 2–6 s from commencement of the trial using 20-ms pulses at 20 Hz produced by a waveform generator (No. 33500B, Agilent, TTL-triggered from the data acquisition board for behavior control). Power density at each fiber tip was ~480 mW per mm^2.

Post hoc immunohistochemistry. One to two months after training, mice were anesthetized (ketamine, 100 mg/kg body weight, and xylazine, 20 mg/kg body weight) and perfused transcardially with 4% paraformaldehyde in phosphate buffer, pH 7.4. After perfusion, tissue was removed from the skull, and the head, including the multi-fiber implant, was additionally fixated in 4% paraformaldehyde for 1 week. The ventral (bottom) side of the skull bone was removed and the brain was carefully extruded. Coronal sections (75–100 µm) were cut with a vibratome (No. VT100, Leica). Before mounting, coronal sections were blocked in 10% normal goat serum (NGS), treated with 1% Triton at room temperature and incubated overnight at 4 °C in 5% NGS, 0.1% Triton and antibodies against glial fibrillary acidic protein (GFAP; mouse monoclonal antibody; 1:500, Sigma No. 032M4779) and Iba1 (rabbit polyclonal antibody; 1:500, Wako Chemicals, No. 019-19471) for astrocyte and microglia staining, respectively. Stained sections were mounted onto glass slides, and confocal images were acquired with an Olympus FV1000.

Registration to the Allen Brain Atlas and tracking of optical fibers. Image processing was performed on grayscale confocal images of the coronal histological sections. To obtain a sharp edge at the brain's midline, we manually segmented all coronal images from the background by using the Lasso segmentation tool of the software Avizo v.9.3.0 (FEI). The preprocessed images were registered in elastix[54] software as follows: one of the central sections containing hippocampus was used as a first reference. The images of two directly adjacent sections (anterior and posterior) were registered to the central image using a two-dimensional rigid-body transformation and the mean-squared difference as similarity measure. Aligned images were then used as references per se to register their adjacent sections. This procedure was repeated until all sections were aligned. Using MATLAB's DIPimage (http://www.diplib.org/dipimage) and tools for NIfTI and ANALYZE image (https://ch.mathworks.com/matlabcentral/fileexchange/8797)[55], we created a 3D NIfTI image for each mouse brain with inter-slice spacing of 0.075–0.1 mm. Each 3D NIfTI dataset was registered to the Allen Mouse Brain volumetric atlas[30] (downloaded from the Scalable Brain Atlas[56]) with the help of Avizo Software. The sharp midline edges of the brains and the atlas[57] reference data provided an additional anatomical constraint, improving the alignment. Registration was implemented in two steps, first using only rigid-body transformations (translation and rotation), then allowing for isotropic scaling and, if needed, additional anisotropic scaling. All registered brain slices were validated by a human. Registrations were based on normalized mutual information[58] as similarity measure and did not allow for shearing transformations. Once the 3D datasets were registered to the reference atlas space, the fiber tracks were manually segmented in each slice using Avizo's Lasso segmentation tool. Three-dimensional reconstructions of these segmentations allowed us to identify fiber ends and obtain their atlas coordinates.

Correlation of calcium signals with whisking and licking. Calcium signals were expressed as percentage ΔF/F. For each trial, the calcium signal was correlated with behavioral variables ('xcorr' MATLAB function). The average whisker angle across all imaged whiskers was measured using automated whisker-tracking software. Whisking was quantified as the mean whisker envelope, calculated as the difference between maximum and minimum whisker angles along a sliding window of 50 ms. Licking was quantified as event rate from the piezoelectric lick sensor. The maximum correlation coefficient within a time lag window of +250 ms was selected. For each of the six mice, we collected correlation coefficients for all expert sessions (fraction of correct trials > 80%).

Network reconstruction. Adjacency matrices were constructed from pairwise correlation coefficients[59]. Cross-correlation values were normalized to zero-lag-time autocorrelations of one (xcorr function in MATLAB). The maximum correlation coefficient within a time lag window of ±250 ms was selected for analysis. To test for significant correlations, we thresholded the cross-correlation matrix by mean ± three standard deviations; mean was calculated from the cross-correlation matrix with shuffled trial labels. Correlation coefficients above threshold were chosen to construct the functional network. To visualize the resulting functional network on a two-dimensional plane, we used a force-directed placement algorithm[60], which is aimed at uniform edge lengths and ensures that nodes that are not connected by an edge tend to be drawn further apart.

Here we assessed functional networks using pairwise correlations between calcium signals as a simple connectivity measure. Other available computational approaches, such as Granger causality[61] and information theory[62], should be directly applicable to photometry data. State-of-the-art computational methods and graph analysis[63] may help to identify characteristic activity patterns in brain-wide circuits.

Analysis of optogenetic perturbation effects on task performance. We applied optogenetic perturbation in thalamic nuclei in four mice. We calculated the percentage of error trials (False Alarms and Misses) as the total number of a particular trial type divided by the total number of trials. We calculated the percentage of error trials separately for trials with and without perturbation, and compared two distributions with a two-sided Wilcoxon signed-rank test.

Mouse tracking. We tracked freely moving mice using custom-written MATLAB code. Video frames were read into a memory pre-allocated data array, which was reshaped according to the coordinates of the arena (specified polygonal region of interest). Image intensity values between minimum and maximum were normalized to a (0, 1) range and binarized with a 10% threshold. To account for several noisy pixels in the data, we removed small objects (areas containing <550 pixels) from the binarized array. Area and centroid coordinates were measured for every frame with the 'regionprops' function. To track two mice, we assigned centroid coordinates to the respective mouse according to the nearest centroid in the previous frame. The Euclidean distance to the object (or the other mouse) was calculated from the respective centroid coordinates. To create occupancy plots, we calculated histogram bin counts of 50 spatial bins (5 × 10) and applied two-dimensional Gaussian filtering ($\sigma = 2$ bins). Peaks in the histogram reflect dwelling spots in the arena and, in the case of two mice, also indicate places of interaction.

Reporting Summary. Further information on research design is available in the Nature Research Reporting Summary linked to this article.

Data availability

The data that support the findings of this study are available from the corresponding authors upon reasonable request.

Code availability

Custom-written software code for data acquisition (LABView) and data analysis (MATLAB) is available upon reasonable request.

References

51. Chen, T.-W. et al. Ultrasensitive fluorescent proteins for imaging neuronal activity. *Nature* **499**, 295–300 (2013).
52. Barnett, L. M., Hughes, T. E. & Drobizhev, M. Deciphering the molecular mechanism responsible for GCaMP6m's Ca^{2+}-dependent change in fluorescence. *PLoS ONE* **12**, e0170934 (2017).
53. Zhao, S. et al. Cell type–specific optogenetic mice for dissecting neural circuitry function. *Nat. Methods* **8**, 745–752 (2011).
54. Klein, S., Staring, M., Murphy, K., Viergever, M. A. & Pluim, J. P. W. elastix: a toolbox for intensity-based medical image registration. *IEEE Trans. Med. Imaging* **29**, 196–205 (2010).
55. Shen, J. Tools for NIfTI and ANALYZE image v.1.27.0.0. *MathWorks File Exchange* https://ch.mathworks.com/matlabcentral/fileexchange/8797 (2014).
56. Bakker, R., Tiesinga, P. & Kötter, R. The Scalable Brain Atlas: instant web-based access to public brain atlases and related content. *Neuroinformatics* **13**, 353–366 (2015).
57. Paxinos, G. & Franklin, K. *The Mouse Brain In Stereotaxic Coordinates* 4th edn. (Academic Press, 2012).
58. Studholme, C., Hill, D. L. G. & Hawkes, D. J. An overlap invariant entropy measure of 3D medical image alignment. *Pattern Recognit.* **32**, 71–86 (1999).
59. Bassett, D. S. et al. Dynamic reconfiguration of human brain networks during learning. *Proc. Natl. Acad. Sci. USA* **108**, 7641–7646 (2011).

60. Fruchterman, T. M. J. & Reingold, E. M. Graph drawing by force-directed placement. *Softw. Pract. Exp.* **21**, 1129–1164 (1991).
61. Seth, A. K., Barrett, A. B. & Barnett, L. Granger causality analysis in neuroscience and neuroimaging. *J. Neurosci.* **35**, 3293–3297 (2015).
62. Ince, R. A. A., Mazzoni, A., Petersen, R. S. & Panzeri, S. Open source tools for the information theoretic analysis of neural data. *Front. Neurosci.* **4**, 62 (2010).
63. Bassett, D. S. & Sporns, O. Network neuroscience. *Nat. Neurosci.* **20**, 353–364 (2017).

nature research

Corresponding author(s): Yaroslav Sych & Fritjof Helmchen

Reporting Summary

Nature Research wishes to improve the reproducibility of the work that we publish. This form provides structure for consistency and transparency in reporting. For further information on Nature Research policies, see Authors & Referees and the Editorial Policy Checklist.

Statistical parameters

When statistical analyses are reported, confirm that the following items are present in the relevant location (e.g. figure legend, table legend, main text, or Methods section).

n/a	Confirmed	
☐	☒	The exact sample size (*n*) for each experimental group/condition, given as a discrete number and unit of measurement
☐	☒	An indication of whether measurements were taken from distinct samples or whether the same sample was measured repeatedly
☐	☒	The statistical test(s) used AND whether they are one- or two-sided *Only common tests should be described solely by name; describe more complex techniques in the Methods section.*
☒	☐	A description of all covariates tested
☐	☒	A description of any assumptions or corrections, such as tests of normality and adjustment for multiple comparisons
☐	☒	A full description of the statistics including central tendency (e.g. means) or other basic estimates (e.g. regression coefficient) AND variation (e.g. standard deviation) or associated estimates of uncertainty (e.g. confidence intervals)
☐	☒	For null hypothesis testing, the test statistic (e.g. *F*, *t*, *r*) with confidence intervals, effect sizes, degrees of freedom and *P* value noted *Give P values as exact values whenever suitable.*
☒	☐	For Bayesian analysis, information on the choice of priors and Markov chain Monte Carlo settings
☒	☐	For hierarchical and complex designs, identification of the appropriate level for tests and full reporting of outcomes
☐	☒	Estimates of effect sizes (e.g. Cohen's *d*, Pearson's *r*), indicating how they were calculated
☐	☒	Clearly defined error bars *State explicitly what error bars represent (e.g. SD, SE, CI)*

Our web collection on statistics for biologists may be useful.

Software and code

Policy information about availability of computer code

Data collection	Fiber photometry data were collected with custom software written in LabVIEW 2013 (64 bit) using a commercial library of functions from Hamamatsu ORCA Flash Video Capture Library and DCAM-API drivers. Software to modulate SLM, Meadowlark Optics.
Data analysis	All data were analyzed in Matlab R2016 b using custom written scripts. The script library for data analysis will be available upon request. Histology slices were segmented in Avizo 9.3.0 (FEI, Hillsboro, Oregon), adjacent coronal slices were registered with elastix software. Using DIPimage and tools for NIfTI and ANALYZE image, a 3D NIfTI image was created and registered to the Allen Mouse Brain volumetric with Avizo 9.3.0. Data distributions were visualized with a modified Violinplot (https://github.com/bastibe/Violinplot-Matlab/) and a notBoxPlot (https://ch.mathworks.com/matlabcentral/fileexchange/26508-notboxplot).

For manuscripts utilizing custom algorithms or software that are central to the research but not yet described in published literature, software must be made available to editors/reviewers upon request. We strongly encourage code deposition in a community repository (e.g. GitHub). See the Nature Research guidelines for submitting code & software for further information.

Data

Policy information about availability of data

All manuscripts must include a data availability statement. This statement should provide the following information, where applicable:

- Accession codes, unique identifiers, or web links for publicly available datasets
- A list of figures that have associated raw data
- A description of any restrictions on data availability

Data will be available upon a reasonable request.

Field-specific reporting

Please select the best fit for your research. If you are not sure, read the appropriate sections before making your selection.

☒ Life sciences ☐ Behavioural & social sciences ☐ Ecological, evolutionary & environmental sciences

For a reference copy of the document with all sections, see nature.com/authors/policies/ReportingSummary-flat.pdf

Life sciences study design

All studies must disclose on these points even when the disclosure is negative.

Sample size	Sample size calculation was not performed. However, there was a consistent increase (3 standard deviations above background) in fluorescence signal upon the stimulus presentation (texture) across all mice. For the 12-fiber experiment we have used 6 mice. Cross-correlation coefficients between calcium dynamics and whisking envelope/licking rate were pooled across 34 expert sessions (percent of correct trials>80%) in 6 mice. For the 48-fiber experiment we have used 3 mice. For each mouse one expert session was presented. To study effects of optogenetic perturbation on behavior we have collected 23 sessions in 4 mice. Resulting performance values (percent of FA and Miss trials) were calculated for trials without and with optogenetic perturbation and compared with a two-sided Wilcoxon signed rank test.
Data exclusions	Only expert sessions were used for the analysis. The exclusion criteria for the expert performance is pre-established (usually expert performance is chosen above 80% of correct trials or d'>1.5). No other criteria was used to exclude data from the analysis.
Replication	Our experimental findings agree with previous studies where cortical calcium dynamics both on the single cell and population level rapidly diverged for Hit and CR trials at the texture presentation onset. Chen, J. et. al. Long-range population dynamics of anatomically defined neocortical networks. Elife 5, e14679, 2016 Gilad, A. et. al. Behavioral strategy determines frontal or posterior location of short-term memory in neocortex. Neuron 99(4):814, 2018
Randomization	The presentation of Go or NoGo (rewarded vs non-rewarded) textures was randomized during texture discrimination task (probability for each texture was 50%). However, same type of texture/trial could not be repeated more then 3 consecutive times. Trials for the opotogenetic perturbation were chosen randomly and with the probability of 30%.
Blinding	Investigators were not blinded. Blinding was not relevant, because the goal of the current study was to develop the method to record the mesoscale brain dynamics.

Reporting for specific materials, systems and methods

Materials & experimental systems

n/a	Involved in the study
☒	☐ Unique biological materials
☐	☒ Antibodies
☒	☐ Eukaryotic cell lines
☒	☐ Palaeontology
☐	☒ Animals and other organisms
☒	☐ Human research participants

Methods

n/a	Involved in the study
☒	☐ ChIP-seq
☒	☐ Flow cytometry
☒	☐ MRI-based neuroimaging

Antibodies

Antibodies used	Astrocytes were stained for GFAP using a mouse monoclonal antibody (1:500; Sigma 032M4779). Clone name G-A-5. Microglia were stained for Iba1 using a rabbit polyclonal antibody (1:500; Wako Chemicals 019-19471). Since Iba1 is a polyclonal antibody the clone name is not apllicable.
Validation	To validate microglial expression, we used a EGFP-expressing CX3CR1 mouse and co-stained against Iba1. The vast majority of microglia cells were co-labeled. Examples of validation experiments and relevant references can be found on the manufacturer's website: for Iba 1 see http://www.wako-chem.co.jp/english/labchem/product/life/AntiIba1/index.htm ; for the GFAP https://www.sigmaaldrich.com/catalog/product/sigma/g3893?lang=de&region=CH

Animals and other organisms

Policy information about studies involving animals; ARRIVE guidelines recommended for reporting animal research

Laboratory animals	In our experiments we used C57BL/6, VGAT-ChR2 EYFP and CX3CR1–EGFP mice. We used male animals of age 2-6 months.
Wild animals	No wild animals were used in our study.
Field-collected samples	No field-collected samples were used.